Characterization of Deltaic Channel Morphodynamics From Imagery Time Series Using the Channelized Response Variance

Teresa Jarriel[1] [ID], **Leo F. Isikdogan[2,3], Alan Bovik[2], and Paola Passalacqua[1]** [ID]

[1]Department of Civil, Architectural and Environmental Engineering and Center for Water and the Environment, The University of Texas at Austin, Austin, TX, USA, [2]Department of Electrical and Computer Engineering, The University of Texas at Austin, Austin, TX, USA, [3]Intel Corporation, Santa Clara, CA, USA

Abstract River deltas are complex, dynamic systems whose channel networks evolve in response to internal and external forcings. To capture these changes, methods to extract and analyze deltaic morphodynamics automatically using available remotely sensed imagery and experimental observations are needed. Here, we apply a promising method for the automatic extraction of channel presence called RivaMap, on both synthetic and experimental data sets, to investigate the changes experienced by the system in response to five changes in forcings. RivaMap is an automated method to extract nonbinarized channel locations from imagery based on a singularity index that combines the multiscale first and second derivatives of the image intensity to favor the identification of curvilinear features and suppress edges. We quantify how the channelization varies by computing the channelized response variance (CRV), which we define as the variance of each pixel's singularity index response through time. We find that increasing magnitudes of sediment inflow (Q_s) and water inflow (Q_w) result in corresponding increases in the maximum CRV. We find that increasing the ratio of Q_s to Q_w results in increased number of channelized areas. We see that adding cohesion to the exposed sediment surface of the experimental delta results in decreased magnitude and decreased number of channelized areas in the CRV. Finally, by observing changes to the CRV over time, we are able to quantify the timescale of internal channel reorganization events as the experimental delta evolves under constant forcings.

1. Introduction

River delta systems are one of the environments most threatened by climate change and anthropogenic activity. Although their low-elevation gradients and fertile soils have made them optimal for human inhabitation and diverse ecologic growth, these characteristics make them susceptible to adverse effects of sea-level rise, flooding, subsidence, and man-made structures such as dams, levees, and dikes. With more than 500 million people living on river delta systems (Giosan et al., 2014), it is important to develop reliable methods to track and predict change in these complex and dynamic systems through time.

The channels that compose river deltas migrate, bifurcate, and avulse to form new networks over time. In order to examine these dynamic networks accurately, high-resolution spatiotemporal data sets and methods to analyze these data sets quickly are needed. High-resolution imagery from various Landsat missions and imagery from river deltas created in experimental basins in laboratory settings have provided the community with useful databases of images to analyze (Connell et al., 2012a, 2012b; Kim & Jerolmack, 2008; Kim et al., 2010; Powell et al., 2012). The community has been able to quantify changes in delta morphology from such data sets; however, analyzing these multispectral images and converting them into data that can be used to quantify changes to delta morphology over space and time in a time efficient manner is a long-standing issue that still remains to be addressed adequately. RivaMap is a tool that has been shown to be able to extract channel presence accurately and automatically from imagery alone (Isikdogan et al., 2015, 2017a). While RivaMap's ability to extract channel presence from single images has been evaluated, the benefits of using RivaMap to track deltaic change through time have not been explored. In this study, RivaMap is applied to imagery of an experimental delta in order to track channel morphodynamics in response to different experimental forcings and a new metric, the Channelized Response Variance (CRV), is developed to quantify these changes in delta morphology through time.

A variety of techniques have been proposed to classify images automatically using diverse satellite sources on a pixel-by-pixel basis for categories such as water (Feyisa et al., 2014; Isikdogan et al., 2017b, 2019; McFeeters, 1996; Pekel et al., 2016; Xu, 2006), lithology (Ninomiya, 2004), vegetation (Tucker, 1979; Carlson & Ripley, 1997), and land use (Fry et al., 2011; Homer et al., 2007; Vogelmann et al., 2001). In order to analyze delta systems, the classified pixels need to be converted into a usable network of channels. There have been a number of methods posed to extract channel centerlines and banks from remotely sensed data, but some are designed to extract single-outlet channel networks and not distributary networks (Costa-Cabral & Burges, 1994; Giannoni et al., 2005; Hancock & Evans, 2006; Lashermes et al., 2007; Montgomery & Dietrich, 1988; Montgomery & Foufoula-Georgiou, 1993; Passalacqua et al., 2010; Pelletier, 2013; Sangireddy et al., 2016; Tarboton et al., 1988), others require digital elevation model data in addition to imagery (Fisher et al., 2013), some use manual delineation techniques to extract the channel bounds and centerlines (Gautier et al., 2006; Schwendel et al., 2015), many require a binary water map to be precreated by the user as input (Güneralp et al., 2013; Pavelsky & Smith, 2008; Rowland et al., 2016; Schwenk et al., 2017), and still others require training data to be provided by the user for the study area of choice (Merwade, 2007). A tool called PyRIS (Monegaglia et al., 2018) automatically extracts channel centerlines from remotely sensed Landsat imagery without requiring the user to first generate a water map. This tool does address some of the limitations of previous methods. However, this tool was designed for meandering patterns, aims to extract only the main channel while avoiding abandoned spurs, and was not tested on more complex branching delta networks whose channels cover a wide range of spatial scales. One aspect many of these techniques have in common is that they extract presence of water in a binary manner. Although this is sometimes appropriate when the boundary between water and land is clear, often in experimental imagery and satellite imagery there are areas where that boundary is more ambiguous. This ambiguity can be seen in regions where there are shallow sediment deposits such as point bars on meander bends or on channel bars in braided systems with no vegetation. It can also be seen in areas with emergent vegetation along the edges of channels that is not dense enough to be considered pure land and not sparse enough to be considered purely wetted channel. Binarizing the channel map results in great loss of information; channels occur in different shapes, sizes, and depths, and representing them all as simply "water" or "land" is too simplistic considering the richness of image detail commonly available today.

To analyze morphodynamic evolution in response to different forcing conditions, we choose to use the RivaMap method for automated extraction of channel presence (Isikdogan et al., 2015, 2017a). RivaMap can take any type of image as input, is capable of extracting distributary networks, requires little user intervention, is able to accurately extract channel presence across a wide range of scales, and, most importantly, is able to represent channel presence in a nonbinary fashion. Instead of representing water presence as a discrete binary data, here water presence is represented in a continuous manner, with higher values indicating areas that are more channelized and lower values indicating areas that are less channelized. Furthermore, it is data independent and computationally efficient in application. By tracking how channel presence changes through time, new insights about the kinematic behavior of delta channels can be gained. In this study, we use both synthetic channel data and an experimental delta basin data set to validate the effectiveness of this image analysis method in analyzing morphological changes over time. It should be noted that in this paper the RivaMap analysis helps to distinguish between channelized flow presence and sheet flow presence in experimental imagery, a distinction that is often difficult to make accurately with set thresholds. It is for this reason that we refer to the RivaMap results as the "channelized response."

The remainder of this paper is organized as follows. We first explain the workflow of the RivaMap method and calculation of the CRV using synthetic data sets as examples (section 2). Then, we describe the setup of the experimental delta and how the images are prepared before the CRV analysis (section 3). We then present the results of the CRV analysis (section 4). A discussion of the results and how they can provide insights into delta morphodynamics follows (section 5). Finally, we state conclusions we have drawn from the outcomes of this study (section 6).

2. RivaMap and the CRV Workflow

There are three major steps in the workflow for this analysis. First, images to be analyzed are acquired and prepared for processing. Next, these prepared images are subjected to the main RivaMap processing to extract the nonbinary channel response, delineate channels, and estimate channel widths. Finally, the CRV analysis is conducted on a collection of multiple images to quantify trends in channel variation over time.
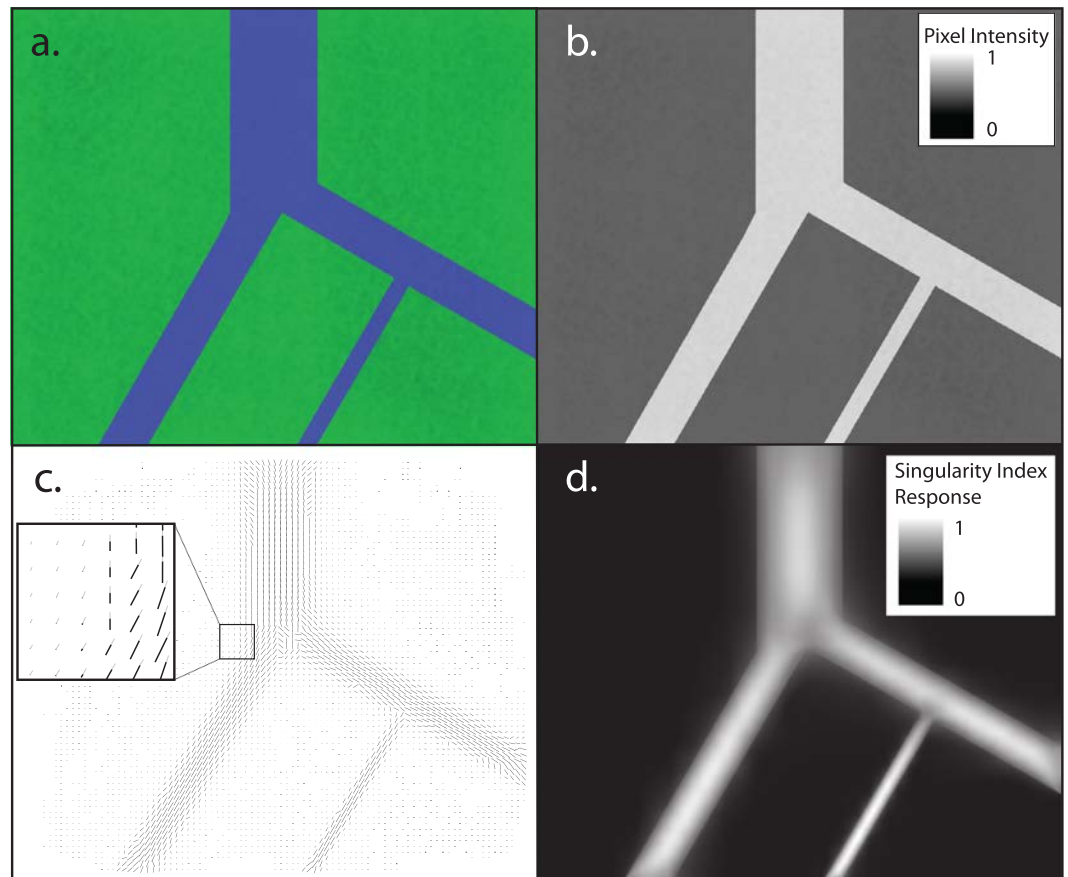
Figure 1. Synthetic analysis for method exemplification. (a) Synthetic RGB network. (b) Example grayscale image from water feature enhancement process on the synthetic network. (c) Quiver plot for the synthetic network showing the direction $\theta_\perp$, the angle perpendicular to the direction θ along which the singularity index is calculated. The length of the quiver lines indicates the magnitude of the singularity index response. (d) Overall singularity index response for the synthetic system.

These three major steps are described in more detail in the following sections using a simplified synthetic color image of a channel network (Figure 1a).

2.1. Preprocessing Image Preparation

RivaMap can take a variety of image types as input. In this study we use images of a physical experimental delta, as well as synthetic channels created using image editing software. Regardless of the input image source, after acquisition, the images are subjected to a water feature enhancement process. The result of the enhancement process is a grayscale image where pixel intensity is higher where water is present (Figure 1b). For instance, if Landsat images are being used, this operation can be done by calculating the Modified Normalized Difference Water Index (MNDWI; Xu, 2006). The MNDWI uses a combination of two multispectral bands to enhance open water features and suppress the soil and vegetation classes. If Red-Green-Blue (RGB) images of an experimental delta with artificially dyed flow paths are used instead, the grayscale image representing the color of the water dye can be extracted by matching the dye color to a band in a defined color space or by using Principal Component Analysis to define a new color space (Bro & Smilde, 2014). In the current release of RivaMap (see Acknowledgments for link to code), the user is provided with the option to input Landsat 5 TM, Landsat 7 ETM+, or Landsat 8 OLI bands for MNDWI computation, input an experimental image with cyan blue dye as the primary water color (section 3.2), or input their own image where the water features have already been emphasized in another manner. RivaMap will provide the best results when the water features have high contrast with other areas, but the method will still work on images in which the water features contrast little with the rest of the image.

2.2. RivaMap Single Image Processing

Once the image has been preprocessed and converted to a grayscale image with water features emphasized, it is then subjected to the main RivaMap processing, which consists of three major components: (i) curvilinear-structure detection using the multiscale singularity index, (ii) channel centerline extraction and delineation, and (iii) channel width estimation. In this study, we focus only on the multiscale singularity index response. For a more detailed explanation of the channel centerline extraction and delineation and the channel width estimation, see Isikdogan et al. (2015), Isikdogan et al. (2017a), and supporting information (section S1).

The multiscale singularity index has been demonstrated to be a highly effective way to automate the extraction of channel features from images (Muralidhar et al., 2013; Isikdogan et al., 2015) and is a combination of low-order multiscale derivatives that are calculated on the intensity of the grayscale input image as

$$(\psi f)(x, y, \sigma) = \frac{f_{0,\theta,\sigma}(x, y) \cdot f_{2,\theta,\sigma}(x, y)}{1 + f_{1,\theta,\sigma}(x, y)^2}, \tag{1}$$

where $f_{0,\theta,\sigma}$, $f_{1,\theta,\sigma}$, and $f_{2,\theta,\sigma}$ are the responses to the zero-, first-, and second-order derivatives of Gaussian kernels at a given scale σ along direction θ (Figures S1a–S1c). The singularity index is designed to respond strongly to curvilinear structures, where the second derivative in the numerator is large, and to respond weakly to edges, where the first derivative in the denominator is large. In equation (1), θ represents the direction of maximum intensity change in the curvilinear mass and is the direction in which the singularity index is calculated. The corresponding direction $\theta_\perp$ represents the direction orthogonal to the direction of maximum intensity change in the curvilinear mass (Figure 1c). Once θ has been determined, the singularity index response is calculated at multiple scales (σ), with the minimum scale being the pixel and its immediate neighbors, and the maximum scale being determined by the image size. The overall singularity index response for each image is calculated by assembling each of the pixel singularity index responses back into a single-band overall response image that highlights the channelized areas across all scales computed on the input image (Figure 1d). This singularity index response map is a nonbinary representation of where channels are located in the system. The nonbinary aspect of the singularity index response is novel in that it does not simply extract the location of water, but rather extracts the strength of the channelized path. In this way, the overall singularity index response can accurately determine the presence of complex and sometimes ambiguous channel presence across the wide range of scales commonly observed in deltas and rivers. Further explanation of the singularity index response calculation can be found in the supporting information (section S1).

2.3. The CRV

When multiple images from different time periods are available, temporal and spatial trends in channel variation can be found by tracking the singularity index response over time (Figure 2). By stacking the singularity index response images from different times and by calculating the variance of each pixel through time, the CRV depicting the areas of the image experiencing the most change in channelization over time may be calculated (Figure 2d). Variance is computed as $s^2 = \frac{1}{n} \sum_{i=1}^{n} (x_i - \bar{x})^2$, where n is the total number of images and x is the singularity index response. Higher CRV values indicate that the pixel experienced larger differences between being identified as a channel and being identified as land. Smaller CRV values indicate that the pixel did not experience significant change between being a channel and being land throughout the time period of observation. Average direction of the CRV is determined for each pixel by conducting a linear-regression analysis on each pixel's time series of singularity index values (Figure 2f). Although the time series of singularity index does not always exhibit a linear trend, the slope of the linear-regression returns accurate information on whether the singularity index is generally increasing or decreasing. Positive slopes indicate that the CRV observed is generally due to an increase in the channelization of the pixel, negative values indicate that the CRV observed is generally due to a decrease in the channelization of the pixel, and slope values near zero indicate that either no change has occurred in the pixel or that there is a nonmonotonic trend to the CRV through time (Figure 2e). By overlaying the CRV map and the slope direction map and observing the trends of directionalized CRV through time, we can begin to make inferences about what geomorphic processes have occurred over the time period of observation (unidirectional lateral migration, oscillating migration, channel widening, channel narrowing, avulsions, etc.).
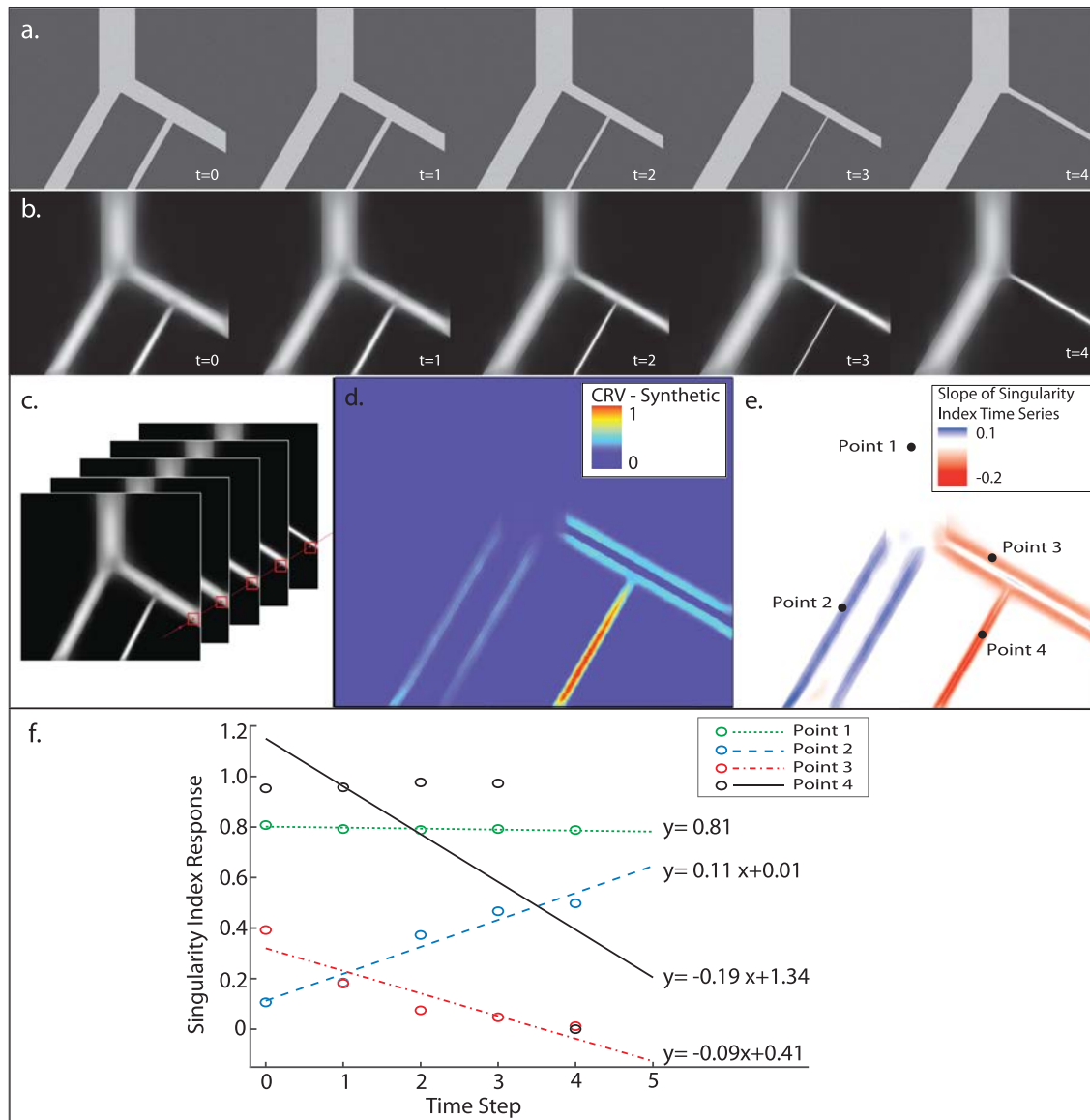
Figure 2. Example channelized response variance (CRV) analysis on synthetic channel network. (a) Five grayscale synthetic images depicting the progression of the left channel enlarging and the right channels decreasing in width and/or completely disappearing, (b) the corresponding singularity index responses, (c) a graphic depicting how the CRV for an example location is calculated from the set of singularity index responses, (d) the final CRV image created, showing no CRV where the channel width did not change, medium CRV where the channels were either widening or narrowing, and high CRV where the channel completely disappeared, and finally, (e) the linear-regression slope values for the singularity index time series that represent the general direction of CRV observed. (f) Example of linear-regression plots calculated from time series of singularity index response for four points is shown in (e).

3. Experimental Delta Setup and Image Preparation

3.1. Experimental Delta Basin

We acquired a set of images from a delta experiment performed at the Saint Anthony Falls Laboratory at the University of Minnesota. The advantages of using data from a physical experiment instead of satellite imagery for this analysis are that, not only is it possible to control the experimental parameters of water input flow rate (Q_w) and sediment input flow rate (Q_s), but we also have imagery available every 30 s and topographic scans taken frequently throughout the experiment. Additionally, physical experimental deltas present the challenge of highly ambiguous channels where it is difficult to objectively determine where a channel ends and sheet flow begins. An advantage of RivaMap is its ability to identify channels using a non-binary parameter, the singularity index response. In imagery of real-world systems and in the experimental deltas meant to model them, there are often ambiguous channels with no clear distinction between land

Table 1
Experimental Delta Cycles

Experiment	Start time	End time	Q_s (L/s)	Q_w (L/s)	Usable images	Number scans
Initial conditions	Hour 0	Hour 31	$4 \cdot 10^{-3}$	0.4	0	0
Cycle 1	Hour 31	Hour 32.5	$2 \cdot 10^{-3}$	0.2	86	2
Cycle 2	Hour 32.5	Hour 34	$6 \cdot 10^{-3}$	0.6	89	2
Cycle 3	Hour 34	Hour 36	$8 \cdot 10^{-3}$	0.4	119	2
Cycle 4	Hour 36	Hour 38	$4 \cdot 10^{-3}$	0.2	119	2
Cycle 5 (hair spray)	Hour 38	Hour 48	$4 \cdot 10^{-3}$	0.2	1218	20

and water. By using this set of experimental images, we are able to demonstrate the ability of RivaMap to deal with such channels and provide a continuous channel response. These benefits make the experimental delta an ideal and nontrivial validation case for the RivaMap method.

We used a 10-m by 10-m basin with water and a mix of anthracite coal and silica sand flowing into the upper left corner of the basin. Water in this experiment was dyed a cyan blue color to aid in the extraction of water presence (Connell et al., 2012a, 2012b; Kim & Jerolmack, 2008; Kim et al., 2010; Powell et al., 2012). The system was run at the initial conditions (Table 1) for 31 hr, until equilibrium conditions were reached. From Hour 31 to Hour 38 (Cycles 1–4), the inflow of water and sediment were modified (Table 1). From Hour 38 to Hour 48 (Cycle 5), the inflow conditions from Cycle 4 were maintained, but the exposed surface sediment sections of the experimental delta were periodically sprayed with hair spray in order to simulate cohesion in the sediment.

From Hour 31 to Hour 38, images of the delta were taken every minute. From Hour 38 to Hour 48 images were taken every 30 s. No images of the delta were taken during the time the delta was reaching equilibrium. For Cycles 1–4, topographic elevation scans were taken at the beginning and end of each cycle of the experiment. During Cycle 5, scans were taken every 12–60 min. Topographic scans were taken by a laser scanner mounted to a mobile system on the ceiling above the basin. Before each scan, the inflow of water and sediment supply to the delta were halted momentarily to drain the channels and to allow bathymetric data to be collected.

3.2. Image Preparation for CRV Analysis

For each cycle of the experiment, an equal number of images at equal spacing were selected. Eighty-six images taken at 1-min intervals were chosen starting from the beginning of each cycle in order to match the temporal resolution of the limiting cycle.

For each image, a grayscale image with the cyan-blue-dyed water emphasized was created by converting the original RGB image (Figure 3a) into a YCbCr color space image. This color space consists of a brightness band Y, a blue-difference chroma band Cb, and a red-difference chroma band Cr. We found that the inverse of the red-difference chroma (Cr^{-1}) was able to enhance the cyan-dyed water regions successfully while suppressing the light and dark sand regions (Figure 3b).

After acquiring a single-band grayscale representation of water presence for each image, all of the images for each cycle were run through the RivaMap processing. For each image, a singularity index response image was generated (Figure 3d). These singularity index responses were then used in the CRV and direction of change analysis (section 4). The benefit of using a nonbinary representation of channel presence can be seen here by comparing the binary water map created by thresholding the grayscale intensity map using Otsu thresholding (Otsu, 1979; Figure 3c) and the singularity index response map (Figure 3d). The nonbinary representation of channel presence is able to discern the strength of channelized features instead of assuming that everything above a threshold is equally channelized.

4. CRV Results

The CRV is a measure of the changing presence of channelized water. In this section, we relate the CRV to physical properties of the system. We expect the CRV to be able to reflect changes in braiding density, channel movement direction, and areas of topographic change (bed aggradation and erosion), because all of
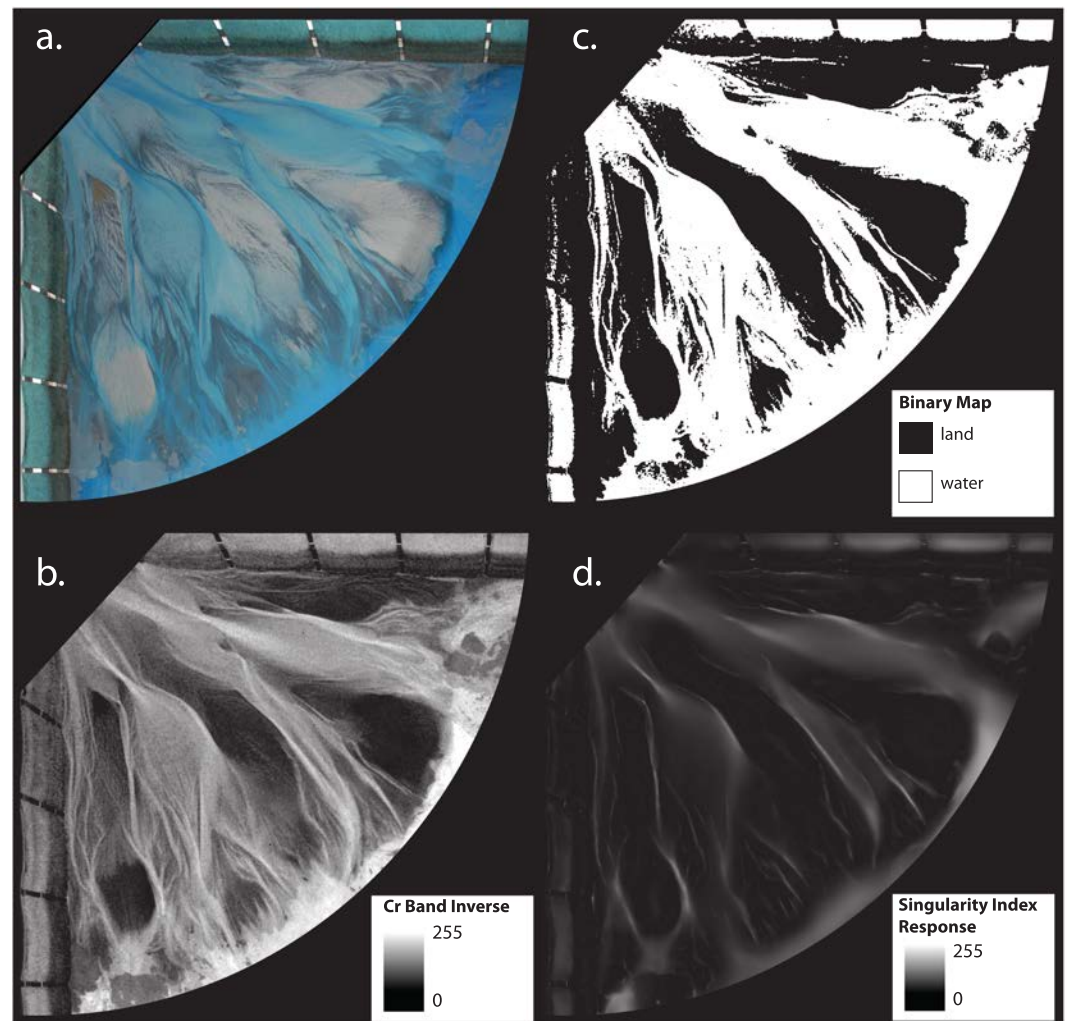
Figure 3. Experimental delta conversion of imagery from (a) RGB color space to (b) Cr inverse color space to represent cyan-blue-dyed water. (c) Binary representation of water and land determined by thresholding grayscale image. (d) Singularity index response map for image (a).

these properties are related to the changing presence of channelized water. These relationships are important to understand because quantifying river delta morphodynamic metrics can be challenging. Linking the CRV to these morphological processes and properties provides a quick standardized method to make inferences about what occurs in the system over varying timescales using only imagery. We also analyze the CRV maps for each of the cycles in order to determine how changing water inflow, sediment load, and sediment cohesion affects the morphodynamics of the system.

4.1. CRV and Channel Braiding Density

In order to assess the relationship between channel braiding density and the CRV, two sections of images from the same cycle (Cycle 5) are separated and analyzed. One section of 43 images from Cycle 5 was chosen because of its relatively low braiding density, while the second section of 43 images from Cycle 5 was chosen because of its relatively high braiding density. Because the images came from the same cycle, all of the images were collected under the same experimental conditions and the amount of water and sediment being delivered to the system was held constant. Braiding density over time is calculated by taking the centerline networks of each image and averaging the number of channels crossing transects chosen at equal spacing across the delta (Figure 4; Ashmore, 1991; Howard et al., 1970). The centerlines are delineated by suppressing the nonmaxima singularity index response along the dominant orientation, which was previously determined (Figure 1c; this portion of the RivaMap method is discussed further in Section S1 and Figure S3). The braiding density value for each of the sections is mapped over time, revealing that the two
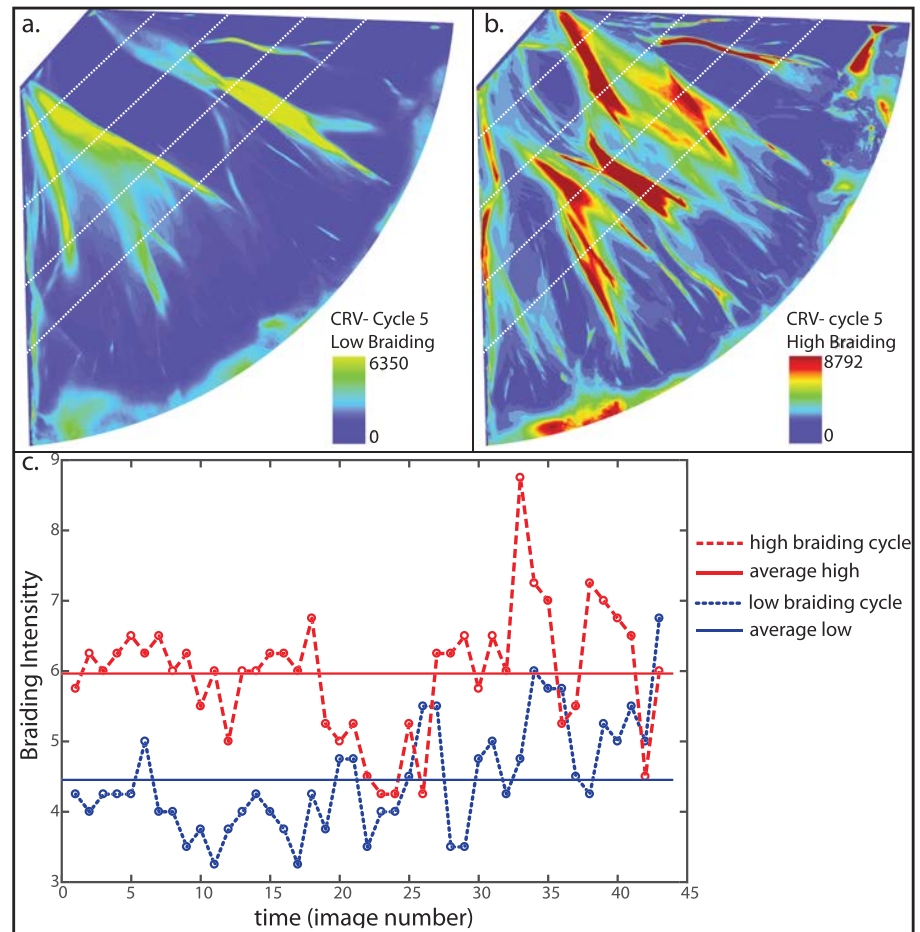
Figure 4. Analysis of CRV and braiding density. CRV map of (a) low braiding density set of 43 images and (b) high braiding density set of 43 images, overlaid with the four transects used to calculate braiding density. (c) Plot of braiding density over time for two sets of 43 images from Cycle 5 of the experiment, with high braiding density images displayed by the dashed line and low braiding density images displayed by the dotted line.

stages of Cycle 5 indeed have different levels of braiding (Figure 4c). The CRV of the experimental delta during each of the two stages is calculated according to the procedure outlined in section 2.3 (Figures 4a and 4b). By comparing the CRV maps to the braiding density patterns for each phase, it can be seen that the stage of Cycle 5 with lower braiding density has a lower overall CRV (maximum of 6,350, mean of 113), while the stage of Cycle 5 with higher braiding density has a higher overall CRV (maximum of 8,792, mean of 137), suggesting that CRV could be an indicator of increased channel activity in the system.

4.2. CRV and Direction of Change

To determine whether the linear regression of the time series of singularity index response is accurately determining the direction of channel movement in the original imagery, the first and last images from the time series (Figure 5a and 5b) are compared to the direction of CRV map for a set of images (Figure 5d). In this particular time series, there are four clearly channelized zones that can be seen in both images. By visually comparing the channel migration we see in the original grayscale images overlaid on top of one another (Figure 5c) to the channel migration observed in the CRV direction map (Figure 5d), we can determine how well the slope of the linear regression represents the direction of channel movement. Here, the terms left and right refer to the directions shown in the lower corner of the imagery (Figure 5).

In Zone 1, the CRV direction map shows strong negative values on the right side of the zone and positive values on the far right of the zone (Figure 5d). This result implies that a strong intensity right channel migrated very slightly to the right. Looking at the overlay of the images at Time step 1 and Time step 2 (Figure 5c), we can see that this is indeed the change that occurred in the system. In Zone 2, the CRV
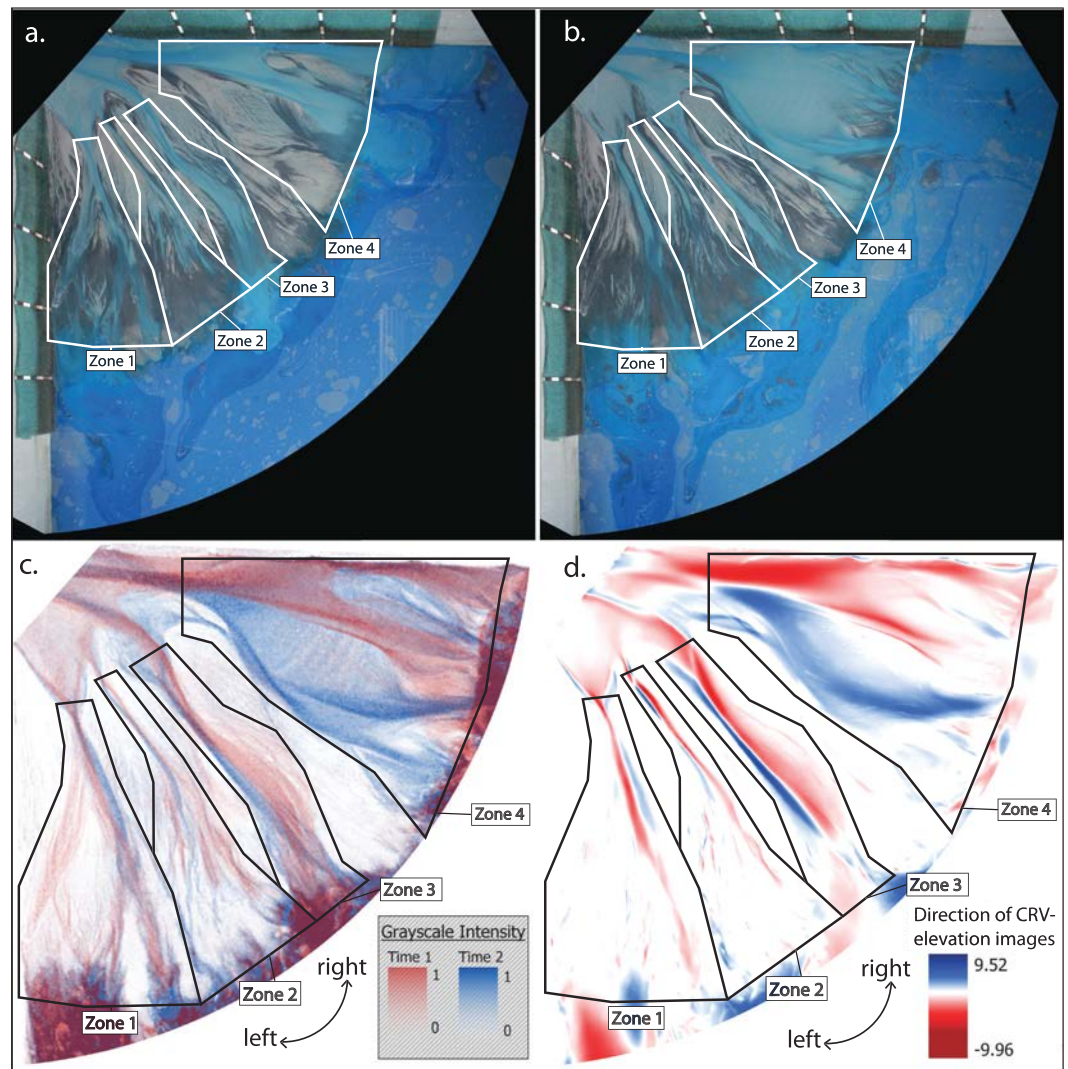
Figure 5. Analysis of CRV direction. (a) RGB image of the experimental delta taken at Time 1, immediately before scan 38.2. (b) RGB image of the experimental delta taken at Time 2, immediately before scan 38.5. (c) Overlay of grayscale intensity maps for Times 1 and 2 to be used for observation of channel movement. (d) Linear-regression slope (CRV Direction) map for all of the images including and in between Times 1 and 2.

direction map shows a strong negative region on the right side with weaker negative values spread toward the bottom, and a thin positive region slightly left of the strong negative region (Figure 5d). This implies that there was a channel present on the right side of the zone that narrowed and moved slightly to the left. Again, comparing the overlay of the grayscale intensity maps (Figure 5c), we see this also in the imagery. Zones 1 and 2 both contain strong negative signals and comparatively weaker positive signals, implying that in these zones, the channelized flow decreased and potentially was diverted to Zones 3 and 4. In Zones 3 and 4, we begin to see stronger and more clear trends. The Zone 3 CRV direction map contains a well-defined wide negative region on the right, and a more narrow well-defined positive region on the left (Figure 5d). From this information, we infer that between Time 1 and Time 2 the channel in this zone migrated left and narrowed slightly. Again, this channel movement is validated by observing the grayscale imagery overlay (Figure 5c). In Zone 4, there is a wide negative region that splits into two thinner negative regions on the right side of the zone, and a wide negative region on the left side of the zone (Figure 5d). Additionally, there is a notable region of no positive or negative slope trend in between the positive and negative regions. This result implies that there was a bifurcated channel on the right side of the zone that then shifted its flow to a new channel to the left. By looking at the grayscale water map overlap (Figure 5c), we see that this does

appear to be the direction of channel movement. From this comparison, we can see that the linear-regression slope maps are accurately representing the direction of channel change in the imagery.

4.3. CRV and Topography

To test whether changes in topography can be detected in the CRV map, the CRV and direction of CRV of the images between Scan 38.2 and Scan 38.5 (Figures 5d and 6a) are compared to the change in elevation between these two scans (Figure 6b). Unfortunately, an exact quantitative comparison of the CRV image and the elevation difference map cannot be produced because the images used to compute CRV were taken at an angle and then orthorectified, and the topographic data were produced by an elevation scanner directly perpendicular to the experimental delta base. Additionally, the patterns of erosion and deposition that cause channel movement are complex and it is not simply the presence of channelized water that determines how and where channels experience geomorphic change. Because of these factors, even if we did have an exact pixel-by-pixel comparison of elevation change and CRV, we might not expect the numerical correlation between CRV and topographic change to be one-to-one. However, in order to simplify the analysis, we hypothesize that in regions where a channel appears (positive values in the CRV direction map), sediment will be eroded as a channel moves into new territory, and in regions where a channel disappears (negative values in CRV direction map), sediment will infill the channel as it is abandoned. General patterns in the similarity between CRV and elevation change can be seen by observing trends in the labeled Zones 1–4 and matching the zones as best as we can between the images (Figure 6).

First, we find that the spatial distribution of the CRV (Figure 6a) and the elevation change map (Figure 6b) are visually very similar. In Zones 1 and 2, for instance, moving away from the inflow point, there is an increasing spatial spread of the zone in both CRV and elevation change. Zones 3 and 4 also have similar spatial structures of the CRV and elevation change. This similarity between the CRV and the elevation change is observed quantitatively by comparing the CRV and the absolute value of elevation change across four transects (Figure 6c). All four transects show similar trends; in general, in areas where there is low CRV, there is also low elevation change, and in areas where there is high CRV, there are spikes in elevation change (Figure 6e). The Spearman rank correlation (Spearman, 1904) for Transects 1–4 are 0.714, 0.694, 0.728, and 0.662, respectively. For every spike in CRV, there are multiple spikes in the elevation difference. These trends can also be seen in the scatter plot comparing normalized CRV and normalized absolute value elevation difference of Transects 1 and 2 (Figure 6d). For each transect, there is a large cluster of points near the (0,0) origin, meaning that there is a large concentration of points where low CRV values and low elevation change values coincide. Both transects also display linear regions where increasing CRV corresponds to increasing elevation change values. Finally, in both transects, for absolute value of elevation change of 0 to 0.3, there is a wide range of corresponding CRV values. This zone represents areas where there is a high CRV and a corresponding low-elevation difference. These points occur due to the occurrence of multiple elevation spikes for each CRV spike. Regardless of these points, there is positive correlation between CRV and elevation change for all four transects.

This positive correlation is further validated by comparing the elevation change (Figure 6b) to the direction of CRV (Figure 5d). Not only is there a similar spatial distribution pattern in all four zones between the direction of CRV map and the elevation change map, but the linear-regression slope analysis is able to pick up the signature of geomorphic change associated with different channel movements. In Zone 1, the direction of CRV map shows strong negative values along one channel and a weaker thin positive value section to the right of the negative channel section (Figure 5d). As stated before, this result implies that there was a channel present that migrated slightly to the right and weakened in intensity. The elevation change map in Zone 1 shows mostly positive values throughout, indicating that smaller channels have been infilled (Figure 6b). Zone 1 does not show any strong new erosion zones aside from a small section near the channel mouth on the right side. This pattern matches what we hypothesized based on the direction of CRV. Similarly, in the direction of CRV map for Zone 2, the most dominant feature is a thin section of negative values (Figure 5d). Parallel to this section of negative values is a thinner weaker section of positive values. As said before, this signature indicates that there was a channel present on the right that migrated slightly to the left and weakened in intensity. Looking at the elevation change map for Zone 2, areas of mostly positive elevation change can be seen, with a few negative elevation changes on the left side of the zone near the channel mouth (Figure 6b). This is the elevation change that we would expect if a strong channel was infilled and migrated leftward as it weakened in intensity. In Zone 3, in the directional CRV map the channel has strong negative values on the right side and strong positive values on the left side (Figure 5d), indicating that
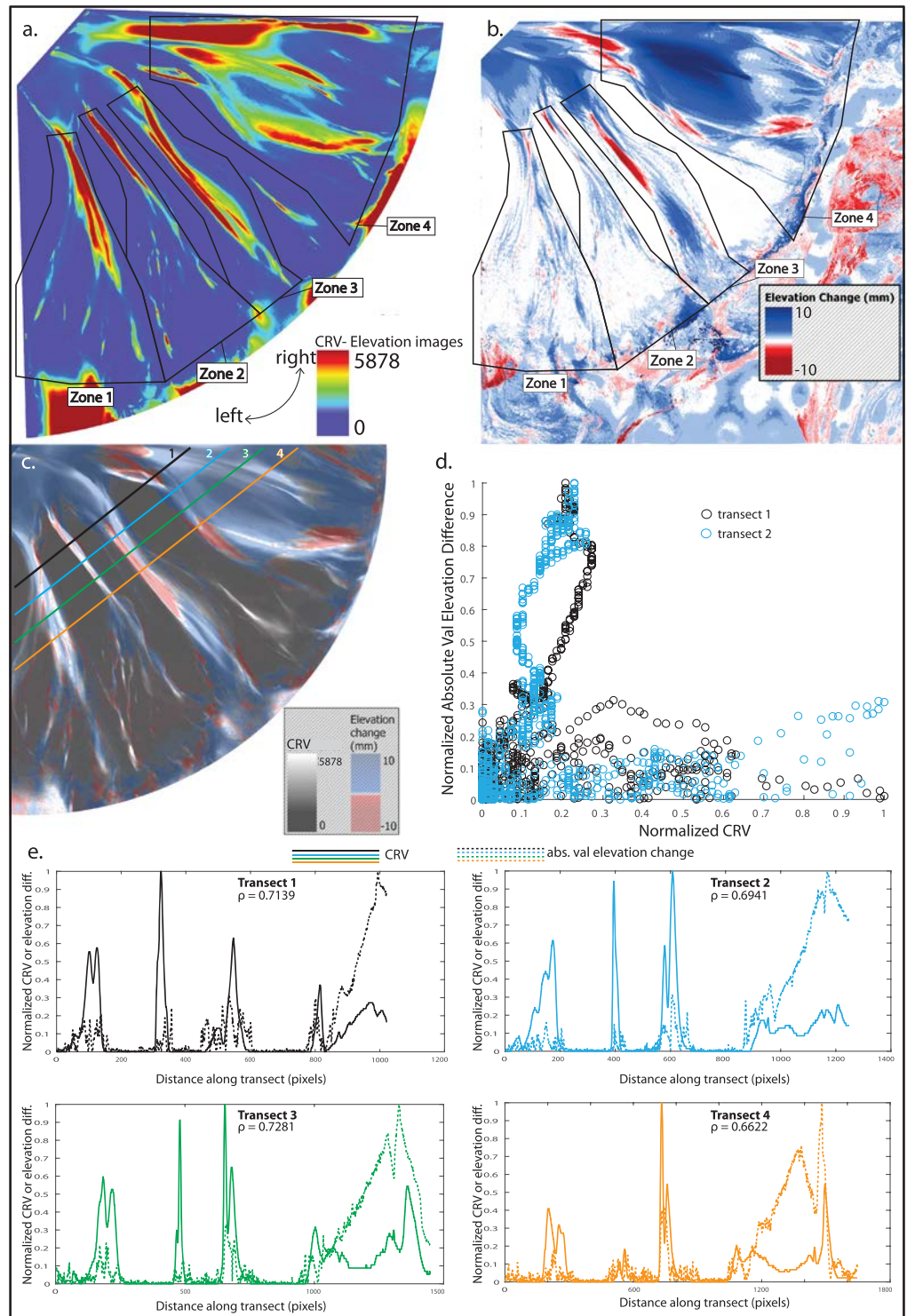
Figure 6. CRV and Topography. (a) CRV for images between Scans 38.2 and 38.5. (b) Elevation change between Scans 38.2 and 38.5. (c) Overlay of (a) and (b) with transects for comparison. (d) Scatter plot of normalized CRV and normalized absolute value of elevation difference for Transects 1 and 2. (e) Values of CRV and elevation change for Transects 1-4.

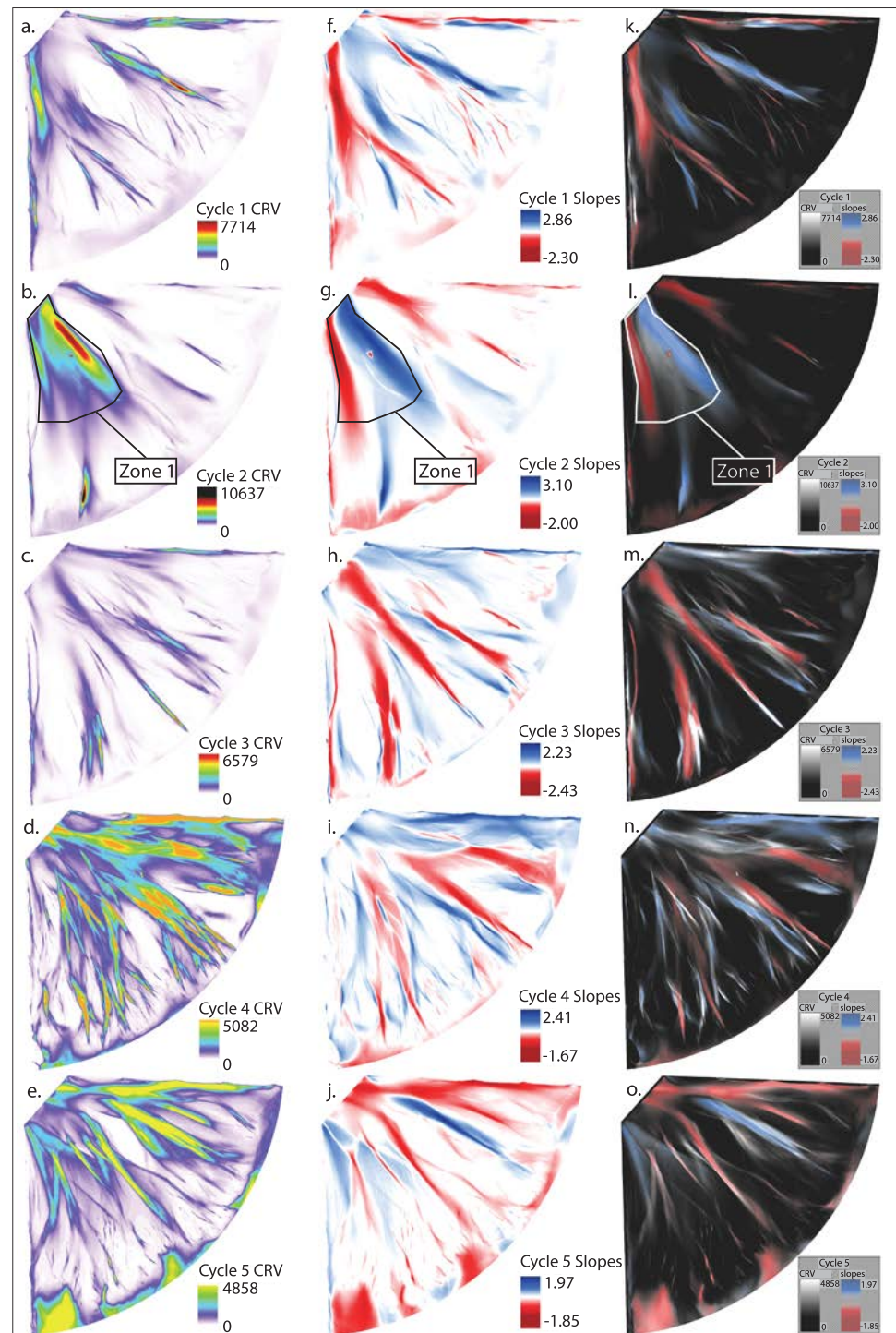**Figure 7.** Comparison of CRV maps, linear-regression slope maps, and overlay of the CRV map and the linear-regression slope map for (a, f, k) Cycle 1, (b, g, l) Cycle 2, (c, h, m) Cycle 3, (d, i, n) Cycle 4, and (e, j, o) Cycle 5 hair spray. The overlays (k, l, m, n, o) show the CRV map for each cycle with a new black to white color scale for clarity with the slope map semitransparent on top.

Table 2
CRV and Direction of CRV for Each Cycle

Cycle	Maximum CRV	Mean CRV	Braiding density of CRV	% positive slopes	% negative slopes
1	7,714	138	5.75	39	61
2	10,637	229	3.25	51	49
3	6,759	102	7.50	59	41
4	5,082	275	9.75	68	32
5	4,858	223	6.75	48	52

the channel has migrated from right to left. If this were the case, we would expect the topography to infill on the right side of the same channel and erode on the left side of the channel as it cuts into new sediment. This is in fact the pattern that we see in Zone 3 for the elevation change map (Figure 6b), indicating that the CRV can predict the areas where we expect the most topographic change to occur, and the direction of the CRV map can identify specific directions of these erosional and depositional patterns. In Zone 4, we see a pattern similar to Zone 3.

Although there is not an exact correlation between elevation change and CRV, the similarities between the outlined zones and the spatial distribution of where the changes are taking place indicate that the CRV analysis could successfully identify areas and directions of changes in topography. It should be noted that these two scans were taken only 18 min apart. If the time between scans increases and the topography is reworked more, then the similarity between the CRV map and the change in topography is expected to decrease.

4.4. CRV and Experiment Stages

With changing experimental conditions, such as inflow rate of water and sediment, it might be expected that the CRV of the system would also change. To test whether the CRV maps could be used to discern differences between the different cycles of the experimental delta (Table 1), we compared the CRV maps for each cycle of the experiment (Figure 7). The bulk results of this comparison are summarized in Table 2.

The different stages clearly have very different CRV maps, both in magnitude of CRV as well as in their spatial patterns (Figures 7a–7e). From Cycle 1 to Cycle 2 there is an increase in the maximum and mean value of CRV and a decrease in the braiding density of the CRV map (calculated in the same as in section 4.1). From Cycle 2 to Cycle 3, there is a decrease in the maximum and mean CRV, but there is an increase in the braiding density of the CRV map. From Cycle 3 to Cycle 4, there is an increase in the number of channelized areas of CRV and an increase in the mean CRV, but there is a slight drop in the maximum value of CRV. From Cycle 4 to Cycle 5, there is a decrease in the maximum and mean CRV and a decrease in the braiding intensity of the CRV map.

We also compare the direction of CRV maps to see if we can use these methods to discern more differences among the five cycles (Figures 7f–7j). Cycle 1's direction of CRV map shows 39% positive values and 61% negative values, indicating that of the CRV that occurred in this cycle, more was due to channels appearing than was due to channels disappearing. Cycle 2 shows nearly equal percentages of positive and negative change (51% positive and 49% negative) indicating that the CRV displayed in Cycle 2 was due equally to channels appearing and disappearing. Cycle 3 shows that 59% of the CRV was in the positive direction and 41% of the CRV was in the negative direction, indicating that in this cycle, CRV was more the result of channels appearing. The direction of CRV map for Cycle 4 shows 68% positive values and 32% negative values, indicating that the CRV for this cycle was due primarily to the appearance of channel features. Finally, Cycle 5 shows more of a balance between positive and negative values (48% positive and 52% negative), indicating that the CRV for this cycle was balanced between channels appearing and disappearing.

To examine how the CRV of each cycle evolves over time, all 516 images from all six cycles are combined into a time-ordered array. A sliding window of size 30 images (corresponding to 30 min of the experiment) is created and run through the 516 images. A 30-image set is chosen as the window size based off of work done in Powell et al. (2012) showing that for a similar physical delta experiment, when the sediment-to-water inflow ratio is 0.015—0.03, the expected autogenic timescale (time between stored sediment release events) is 35–50 min. We chose a value below the minimum of 35 min in order to attempt to isolate the expected events in the CRV and chose 30 min as the window (as opposed to even lower values) in order to guarantee
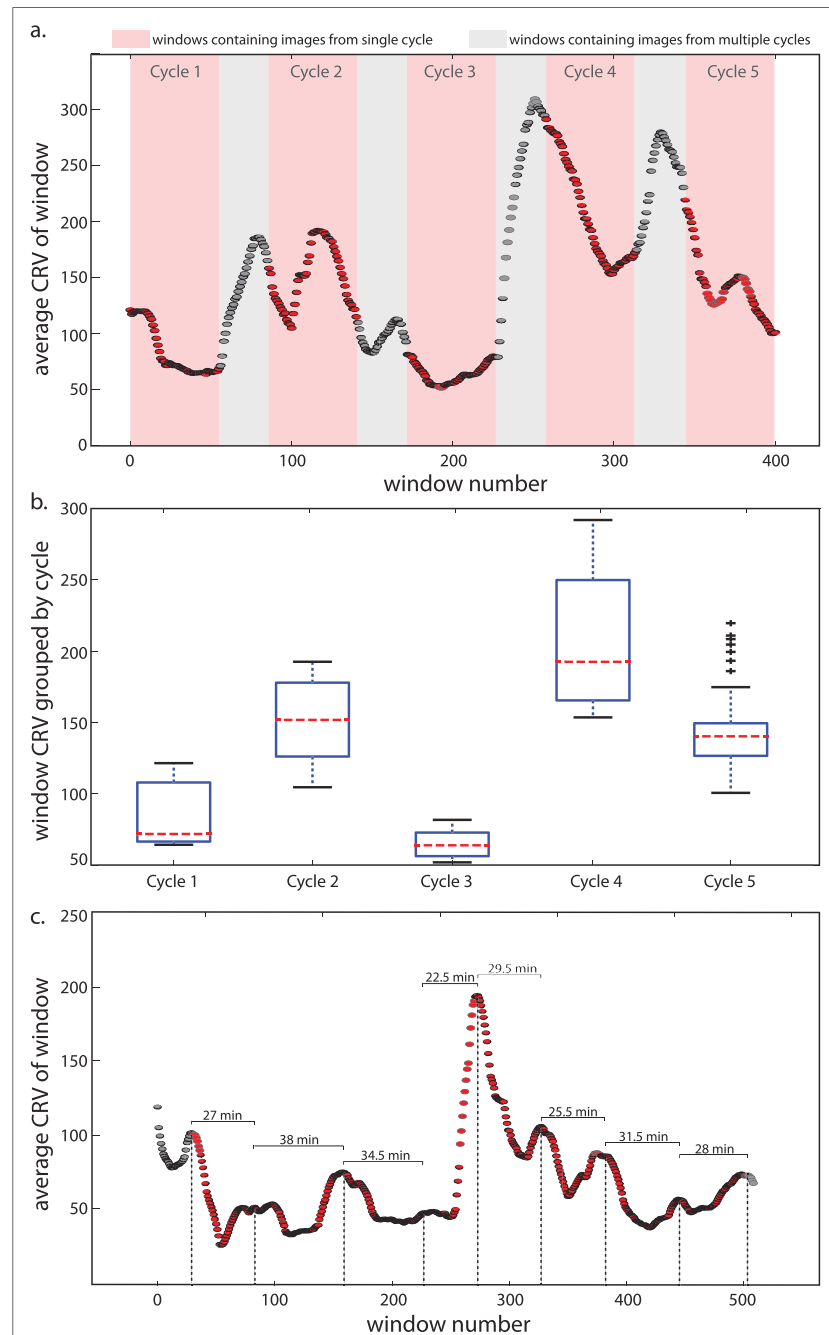
Figure 8. Sliding window CRV analysis. (a) Average CRV values of each of the sets of 30 images as window slides through time. (b) Standard box plot distribution of average CRV values for each set of images separated into cycles. (c) Sliding window analysis for Cycle 5 Hours 43–48.

a sufficiently large sample size for the CRV calculations. For each window of 30 images, the average CRV is calculated and plotted (Figure 8a). One can see patterns in the amplitude and periodicity of the CRV spread when the windows are separated into their cycles. There appear to be gaps between the cycles because we only counted a window to be part of a cycle if it only contained images from that single cycle. The windows that do not belong to any cycle in the plot are those that contain some images from the previous cycle and some images from the next cycle, and therefore reflect a mix of forcings. The images from Cycle 1 show high average CRV in the beginning and then low average CRV values toward the end, implying that there was a short interval of large amount of change before the system stabilized. Cycle 2 shows a period of decreasing

average CRV followed by a peak in average CRV and then another decrease. This implies that in Cycle 2 the delta experienced a fluctuation in its channel network in the middle of the cycle, but by the end of the cycle it began to return to a constant state. Cycle 3 shows comparatively low average CRV values than the other cycles. There is a slight decrease in the average CRV in the middle of the cycle and a slight increase toward the end of the cycle, but the low magnitude of these values implies that the change occurring was not as large as changes observed in Cycles 1 and 2. Cycle 4 shows a large decrease in average CRV as the cycle progresses, with a slight increase in average CRV toward the end of the cycle, implying that this cycle was beginning to experience a substantial geomorphic change, but was potentially unable to complete it before the inflow conditions were altered. Finally, Cycle 5 shows a decrease in average CRV followed by a small peak in average CRV, indicating that there was a change in the channel presence midcycle.

Once the cycles are imposed on the data, the points are grouped into their respective cycles and a box plot is created of the CRV points falling within each cycle (Figure 8b). We find that the overall magnitude of the CRV and the interquartile range of the CRV are different for each of the cycles, implying that the CRV over time can discern different phases of an experiment. Mean CRV increases from Cycle 1 to Cycle 2 and decreases for Cycle 3. CRV is highest for Cycle 4 and decreases for Cycle 5. The interquartile range of the CRV values also follows the same pattern.

A similar analysis was also conducted on 545 images from Hour 43 to Hour 48 of the Cycle 5 experiment (Figure 8c). With a longer time period of observation, we are able to use the CRV analysis to visualize the periodicity of changes occurring in the delta when inflow conditions are held constant. Again, the images are combined into a time-ordered array, a sliding window of 30 images is created and run through the images, and the average CRV value for each window is plotted (Figure 8c). Here, imagery was available every 30 s, so the 545 images represent 4.5 hr of running experiment. There are multiple peaks in this time series of CRV. Many peaks have similar amplitudes, while there is one peak with an amplitude much larger than the rest, indicating a larger change occurring in the system. Peaks in CRV occur every 22.5–38 min for this section of Cycle 5, and the average time between CRV events is 29.5 min.

5. Discussion

Even in this controlled experimental setting, the delta systems we observe are complex networks that can change rapidly in response to changes in sediment and water inflow rates. In real-world delta systems, in addition to changing sediment and water inflow rates, delta channel networks are also potentially evolving in response to changes in land use, anthropogenic fluvial modification structures, subsidence, and modern climate. The scientific community is in need of state-of-the-art methods capable of quantifying changes in delta morphology quickly and accurately. The CRV is a novel metric that allows us to analyze the magnitude and mechanisms of geomorphic change in these complex delta systems. Here, we discuss how the CRV method can be used to analyze delta morphodynamics and how the nonbinary aspect of the CRV method provides more information than the variance of the imagery itself or a binarized representation of the imagery.

5.1. CRV as an Indicator of System Properties

The results of the temporal singularity index analysis suggest that the CRV can track changes over time in complex delta systems. The results presented in section 4.1 show that increases in the CRV of a system could be correlated to channel mobility as measured by braiding density. This finding is useful, because calculating braiding density manually on multiple images can be time consuming and measuring how "active" a delta is can be a difficult task. Using the CRV as a proxy for channel mobility can be an effective and objective solution. The CRV expands upon what the braiding density can tell us because instead of simply having a single bulk number representing the activity of a system, we now have a spatially distributed representation of change in the system as well.

The results from section 4.2 suggest that the linear-regression slope analysis is able to determine accurately the direction of change in the singularity index response. The results from section 4.3 show that changes in topography between two time steps are captured by the CRV and the linear-regression slopes for the images between the same two time steps. This matching spatial distribution of CRV and elevation change makes sense because the presence of water flow carrying sediment is what drives geomorphic change. It follows that if the CRV is designed to track changes in the location of channels, it can also track where elevation changes occur. However, as we noted, the CRV and elevation change are not perfectly correlated. For every CRV peak in the transect (Figure 6e), there are multiple peaks in the elevation change, which are

usually due to the fact that part of the channel is experiencing erosion, part of the channel is experiencing deposition, and the rest is not experiencing any elevation change. These results lead us to conclude that although CRV cannot be used as a direct representation of elevation change, in situations where repeated high-resolution topography scans are not available, the CRV can be used to represent and limit the area over which elevation change could be expected to occur. If the direction of elevation change is needed and unknown, then the linear-regression slope map can be used to estimate the expected direction of channel movement and elevation change. In this case, the CRV does not provide new information that the elevation data cannot. Instead, it provides a method by which to approximate elevation changes. The relationship between elevation change and CRV could have important implications for stratigraphy as what we see on the surface from imagery could help us roughly model the subsurface structure.

5.2. CRV and Cycle of the Experiments

The differences in the CRV intensity, spatial distribution, and temporal distribution for the different cycles of the experimental delta imply that the CRV analysis could be a way to discern the different regimes of a delta system undergoing natural or anthropogenically forced changes.

When discussing Cycles 1–4 of this experiment it is helpful to consider the autogenic timescale, which is the timescale between storage and release events in a system. The autogenic timescale has been found to respond strongly to the sediment inflow rate, the water inflow rate, and the ratio between the two (Kim & Jerolmack, 2008; Powell et al., 2012; Van Dijk et al., 2009). In general, as the supply of sediment increases in the system, there is more sediment available to fill the available space more quickly, resulting in a decrease of the autogenic timescale between release events that can reorganize the system. As the supply of water increases, more organized systems with more defined channels form, increasing the autogenic timescale between release events. Because we studied each of the cycles for the same amount of time, an increase in the autogenic timescale would indicate fewer cycles of release and storage and thus less change occurring in the system. Here we use these patterns to attempt to explain how the CRV may be used to characterize the autogenic timescale of a system.

The experimental conditions for this experiment allow for the analysis and comparison of three sets of cycles. First, we have a case where Q_w remains constant, and Q_s increases (Cycles 1 to 4). With this change, the increase in sediment should decrease the time it takes for channels to fill and decrease the time between release events. With more release events occurring, the mean CRV should increase when comparing the CRV of Cycle 1 and Cycle 4. We also would expect there to be more channelized areas of the delta experiencing variability as new channels are formed more frequently. Looking at the CRV for Cycle 1 (Figure 7a) and Cycle 4 (Figure 7d), we find that the mean CRV is higher for Cycle 4 than it is for Cycle 1, and the braiding density of the CRV for Cycle 4 is higher than for Cycle 1. A second case that can be analyzed in this experiment is what happens when the ratio of sediment to water (Q_s/Q_w) is adjusted. In Cycles 1 and 2 $Q_s/Q_w = 0.01$ and in Cycles 3 and 4 $Q_s/Q_w = 0.02$. An increase in this ratio means that there is relatively more sediment supply and less water, both of which act to decrease the autogenic timescale and increase the CRV. One result of this increase in ratio is an increase in the braiding density of the CRV maps as new channels are formed more frequently. There is an increase in braiding density when comparing Cycles 1 and 2 to Cycles 3 and 4 (Table 2). Finally, we can analyze how changing the magnitude of Q_s and Q_w while keeping their ratios constant affects the CRV of the systems by comparing the changes we see from Cycles 1 to 2 and Cycles 4 to 3. Here, we see that increasing the magnitude of sediment and water inflow while keeping the ratio constant results in an increase in the maximum CRV (Table 2). This could be because as the sediment and water supply are increased, deeper channels with larger singularity index responses can be created and cause greater overall magnitudes of CRV.

While observing the spatial distribution of the CRV between the cycles is telling, another way to analyze channel morphodynamics is to look at the CRV of a single cycle as it occurs over longer time spans. This allows us to see multiple release events and provides information on the periodic nature of river delta reorganization. This is seen by looking at the scatter plot of the 545 images taken between Hours 43 and 48 of the Cycle 5 experiment (Figure 8c). Here we see multiple peaks spaced relatively evenly, every 22.5–38 min apart. From this we can assume that the autogenic timescale of Cycle 5 is somewhere between 22.5 and 38 min. The average time between release events is 29.5 min. Similar times between release events were found by repeating the analysis with other window sizes (15, 20, 25, 35, 40, 45, and 50 images per window).

This could be applied to other imagery as another analysis that can be used to determine the response of deltas to changes in experimental conditions.

These results demonstrate how the CRV maps and their corresponding linear-regression slope maps can be a useful tool with which to analyze a property such as the autogenic timescale. In experimental deltas, changes in the shoreline of the system are used to measure the timescales of storage and release processes (Kim & Jerolmack, 2008; Powell et al., 2012; Reitz et al., 2010; Van Dijk et al., 2009). If this method were paired with the CRV analysis, the spatial distribution of autogenic processes along with the timescale of autogenic processes could be produced. This information is important in order to separate allogenic and autogenic signatures in the subsurface stratigraphy.

Lastly, when Cycle 4 is compared to Cycle 5, there is a clear decrease in both the mean value and braiding density of the CRV between the cycles. This decrease occurred as anticipated because Cycles 4 and 5 had the same inflow conditions, but Cycle 5 had hair spray continuously applied to the exposed sediment. We expected the hair spray to increase the cohesion of the sediment and to stabilize the delta, and according to this CRV analysis, the hair spray did have that predicted effect. The increased cohesion also can be observed in the direction of CRV maps (Figures 7i and 7j). From Cycle 4 to Cycle 5, as exposed sediment became more cohesive, we see the direction of CRV values change from 68% positive and 32% negative, to 48% positive and 52% negative. This result shows that as cohesion increased, the system stopped forming new channels as often as before and began to have more of a balance between new channels forming and old channels infilling.

In this paper, we use the CRV and its direction to quantify how the morphodynamics vary for systems experiencing different water and sediment inflow rates and different sediment cohesion. However, this metric could also be applied to other experiments in the future to help answer questions about delta evolution such as how the magnitude and spatial distribution of channel kinematics differ with different sediment compositions, different subsidence rates, implementing different manmade structures at various points in a delta, the periodicity of storm events, or vegetation density. Any experiment that contains nonstationarity in the conditions can use the CRV metric to analyze change over time in a system. Additionally, any experiment with stationary conditions that seeks to understand the periodic nature of reorganization events in fluvial systems could use the CRV metric to quantify change.

5.3. CRV and Channel Migration

In addition to the linear-regression slope map allowing us to see where the water appears and where it disappears, combining the slope map with the CRV map allows us to determine how the change occurs. For example, let us pair two scenarios. The first is Cycle 2 of the experiment. In Cycle 2 (Figure 7b), on the leftmost side of the delta, labeled Zone 1, CRV is high. The direction of CRV for this cycle (Figure 7g) shows negative slopes on the left side of Zone 1, positive slopes on the right side of Zone 1, and slopes near zero in the middle, indicating that a channel disappeared on the left side of the zone and appeared on the right side of the zone. Overlaying the slope on top of the CRV (Figure 7l) shows that there is high CRV under and between the area of negative slope and that of positive slope of Zone 1. This result implies that the area in between experienced a large CRV, without clear direction. Such a scenario would occur if the channel migrated laterally from left to right. The values on the left would begin with high singularity index values and end with low singularity index values, creating the negative trend to the linear-regression analysis. The values on the right would begin with low singularity index values and end with high singularity index values, creating a positive trend to the linear-regression analysis. The area in the middle of the two zones would begin with low singularity index values, transition to high singularity index values as the channel passes over, and end with low singularity index values as the channel moves further right. This pattern of low, high, low would leave the area with a high CRV value, but a linear-regression slope trending near zero. We see this signature in the maps of Cycle 2, so without even seeing the original imagery, from just the CRV and linear-regression slope maps, we can determine how the channel migrated.

The second scenario is that of a channel that does not laterally migrate to change location, but rather avulses. An example of this form of migration can be seen looking at the imagery between Scans 38.2 and 38.5 (Figures 5 and 6). In Zone 4 there is a similar pattern in the linear-regression slopes: negative values on one side and positive values on the other with a zone of near-zero slopes in between (Figure 5d). Here, though, CRV is high where there are positive and negative slope values and is low between them (Figure 6a). This result indicates that the area between the positive and negative linear-regression slopes did not experience

a change in singularity index response, as in the case of a channel moving from right to left by avulsing at the point where the channels meet upstream. Again, we are able to discern how the geomorphic change happened without needing to look through the entire set of the imagery and by only using the CRV and linear-regression slope maps.

Other geomorphic processes would have their own unique signatures in the CRV and linear-regression slope maps as well. For instance, if a channel were to widen, the CRV map would show low values in the middle and high values on either side (Figure 2d), and the linear-regression slope map would show a value of zero (or negative if the channel strength is decreasing as the channel widens) in the middle and positive slopes on either side (Figure 2e). If a channel were to narrow, the CRV map would be similar with low values in the middle and high values on the edges, but in this case the linear-regression slope map would show values of zero in the middle and negative slope values on either side. If a channel were to bifurcate, the CRV map would show three distinct channelized areas of high CRV with low CRV between them. The middle channel would show negative direction of CRV and the outer channels would show positive directions of CRV. The expected CRV signatures of the various geomorphic processes discussed, as well as other potential processes we did not necessarily see in this experiment, are summarized in Table S1 in the supporting information.

Knowing these signatures of geomorphic change, we can now say that in general Cycle 1 was dominated by avulsion events since there are mostly paired positive and negative values with low CRV between them (Figure 7k). As discussed in the example, Cycle 2 is dominated by lateral migration (Figure 7l). Cycle 3 appears to be dominated by channel bifurcations as there are multiple points where we see negative slope values in the middle and positive slope values on the edges of the channels with areas of low CRV between the channels (Figure 7m). The methods of channel migration are not as clear for Cycles 4 and 5 because this analysis requires there to be clear pairs of positive and negative CRV zones. For Cycles 4 and 5, there is no clear pairing because so many new channels were formed and so many old channels were infilled. Cycle 4 shows around three channels infilling and around eight channels forming (Figure 7n). Cycle 5 shows around five channels infilling and three new channels forming (Figure 7o). In these cases, if the methods of channel migration were desired, the time series of imagery would need to be examined to manually match the infilled and newly formed channels.

5.4. CRV Compared to Variance of Grayscale and Binary Imagery Time Series

It has been shown that the CRV response is a method by which imagery from different cycles of an experiment can be compared to one another. It is also a method by which one can identify geomorphic change quickly from imagery alone without needing to watch a video of the delta evolution and identify change by eye. In order to determine whether analyzing the CRV tells us more information than simply analyzing the variance of the Cr^{-1} grayscale water emphasized images, a comparison of the two variance images was conducted for Cycles 4 and 5. We also compared the variance of binarized images from these cycles to determine whether the nonbinary aspect of the singularity index response was important.

We find that the CRV depicted change in channels much more clearly than the grayscale imagery and the binary imagery. This can be seen by comparing the CRV of Cycle 4 (Figure 9a) and Cycle 5 (Figure 9d) to the variance of the grayscale Cr^{-1} imagery of the images for Cycle 4 (Figure 9b) and Cycle 5 (Figure 9e) and to the variance of the binary imagery for Cycle 4 (Figure 9c) and Cycle 5 (Figure 9f). In the CRV imagery, there are clear channel-like zones where changes in the presence of channelized water were detected. We do not see those clear channelized zones in the variance of the grayscale imagery or the variance of the binary imagery. This is because the singularity index is not simply identifying the presence of water. Rather, it is determining the strength of the channelized response in imagery. This is important because the singularity index allows us to track the direction of migration of specific channels over the course of the entire experiment. The lack of clarity as to what is or is not a channel in the grayscale variance does not allow us to resolve migration direction. The binarized images contain even less clarity than the grayscale imagery because they are erasing many signatures of channels by assuming that every pixel above a defined threshold is equally channelized.

We also found that the variance of the grayscale images and variance of the binary images were unable to show the same difference in magnitude of variance between Cycles 4 and 5 that the CRV was able to capture. Cycles 4 and 5 had the same conditions, except for Cycle 5, hair spray was added to the experiment to simulate cohesion of the exposed sediment. Looking at the imagery from the cycles, the increased cohesion appeared to stabilize the channel locations and decrease the number of new channels being formed (decrease the braiding density of the CRV map). The CRV showed us a decrease from Cycles 4 to 5 in both the
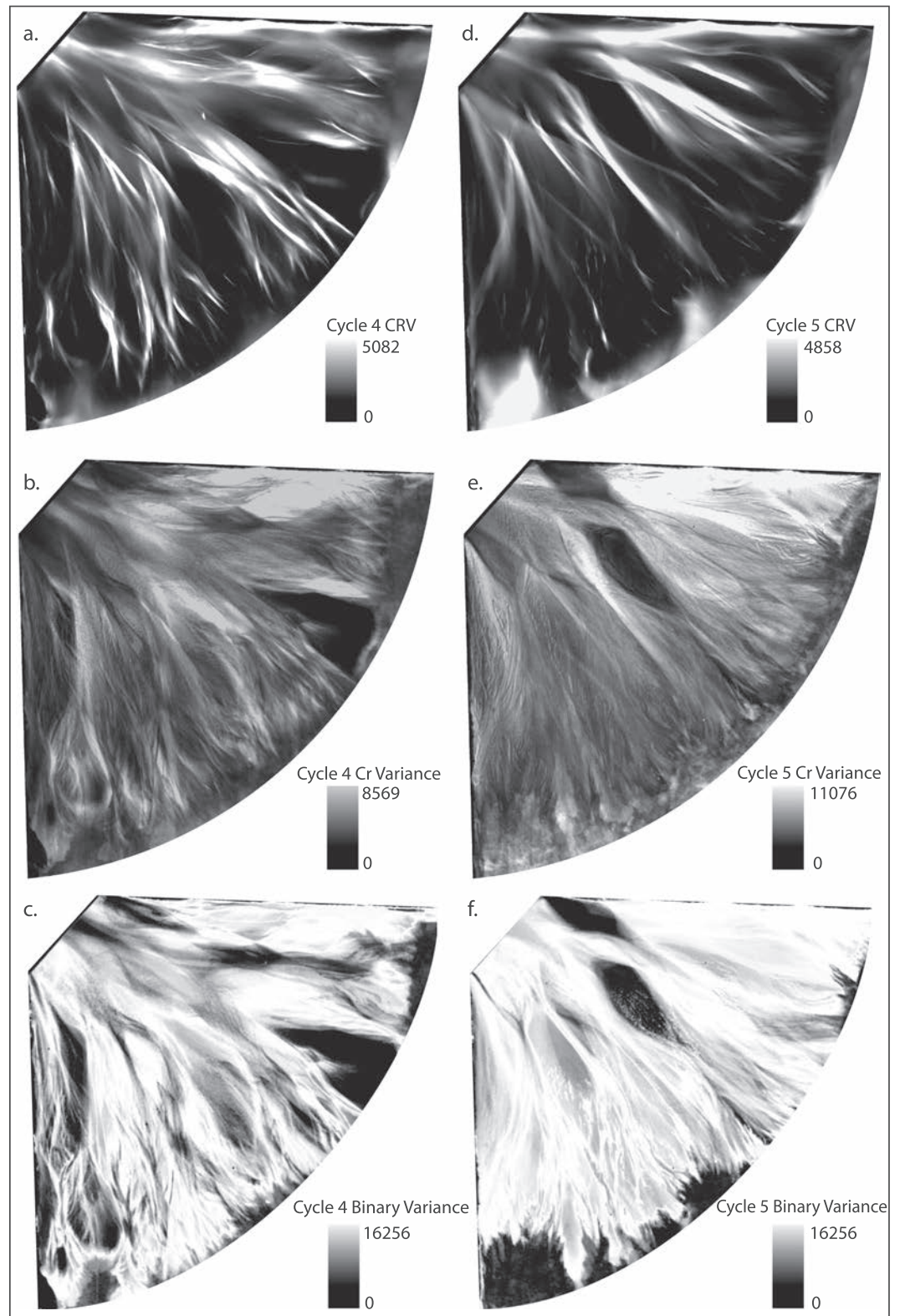
Figure 9. CRV for (a) Cycle 4 and (d) Cycle 5 images. Variance of the grayscale Cr inverse map for (b) Cycle 4 (e), and Cycle 5 images. Variance of binary imagery created by thresholding the grayscale imagery at the 60th percentile for (c) Cycle 4 and (f) Cycle 5 imagery.

magnitude of the CRV as well as the number of channels experiencing CRV. The grayscale variance, however, did not show us the decrease in magnitude and was unable to show the decrease in number of channels experiencing morphological change from Cycles 4 to 5. In fact, the grayscale imagery variance showed an increase in variance magnitude from Cycles 4 to 5. The binary image variance for Cycle 4 (Figure 9c) and Cycle 5 (Figure 9f) showed equal maximum variance values and the spatial distribution of the variance did not allow for us to distinguish between the two cycles.

6. Conclusions

With hundreds of millions of people living on river delta systems throughout the world (Giosan et al., 2014), it is important to improve our understanding of deltas and how their channel networks will change in response to internal and external forcings. The methods introduced in this paper will allow the community to analyze delta morphodynamics more quickly and more accurately than before. We have shown that the singularity index response accurately identifies channel location in a nonbinary fashion. We also proposed and tested the CRV, a new metric for tracking change in the channel system through time, which is calculated by compiling multiple images and calculating the variance of the singularity index response at each pixel. The CRV metric proved to be effective at discerning changes in topography, changes in the activity of channels, and changes in the inflow parameters to the experiment. In addition, by adding direction to the CRV in the form of the linear-regression slope map, we have proposed a method to identify not only what areas are changing, but also in which direction they are moving. Lastly, overlaying the CRV and linear-regression slope can provide new information about the geomorphic processes altering the delta system. By applying these analyses to experimental deltas experiencing different external forcing, we find that increases to the ratio of sediment inflow to water inflow result in larger CRV braiding densities (more areas of CRV occurring). We find that the maximum CRV achieved in a system is positively related to the magnitude of the sediment and water inflow. We also find that the addition of a stabilizing agent (hair spray) to the exposed sediment of an experimental delta stabilizes the channels and reduces the number of channelized areas in the CRV. All of the analyses introduced in this paper can be used in other experiments to track channel morphodynamics of river deltas as they evolve through time.

References

Ashmore, P. E. (1991). How do gravel-bed rivers braid? *Canadian Journal of Earth Sciences*, *28*(3), 326–341.

Bro, R., & Smilde, A. K. (2014). Principal component analysis. *Analytical Methods*, *6*, 2812–2831. https://doi.org/10.1039/C3AY41907J

Carlson, T. N., & Ripley, D. A. (1997). On the relation between NDVI, fractional vegetation cover, and leaf area index. *Remote Sensing of Environment*, *62*(3), 241–252.

Connell, S. D., Kim, W., Paola, C., & Smith, G. A. (2012a). Fluvial morphology and sediment-flux steering of axial transverse boundaries in an experimental basin. *Journal of Sedimentary Research*, *82*(5), 310–325. https://doi.org/10.2110/jsr.2012.27

Connell, S. D., Kim, W., Smith, G. A., & Paola, C. (2012b). Stratigraphic architecture of an experimental basin with interacting drainages. *Journal of Sedimentary Research*, *82*(5), 326–344. https://doi.org/10.2110/jsr.2012.28

Costa-Cabral, M. C., & Burges, S. J. (1994). Digital elevation model networks (DEMON): A model of flow over hillslopes for computation of contributing and dispersal areas. *Water Resources Research*, *30*(6), 1681–1692.

Feyisa, G. L., Meilby, H., Fensholt, R., & Proud, S. R. (2014). Automated water extraction index: A new technique for surface water mapping using Landsat imagery. *Remote Sensing of Environment*, *140*, 23–35.

Fisher, G. B., Bookhagen, B., & Amos, C. B. (2013). Channel planform geometry and slopes from freely available high-spatial resolution imagery and DEM fusion: Implications for channel width scalings, erosion proxies, and fluvial signatures in tectonically active landscapes. *Geomorphology*, *194*, 46–56.

Fry, J., Xian, G. Z., Jin, S., Dewitz, J., Homer, C. G., Yang, L., et al. (2011). Completion of the 2006 national land cover database for the conterminous United States. *Photogrammetric Engineering and Remote Sensing*, *77*, 858–864.

Gautier, E., Brunstein, D., Vauchel, P., Roulet, M., Fuertes, O., Guyot, J. L., et al. (2006). Temporal relations between meander deformation, water discharge and sediment fluxes in the floodplain of the Rio Beni (Bolivian Amazonia). *Earth Surface Processes and Landforms*, *32*(2), 230–248. https://doi.org/10.1002/esp.1394

Giannoni, F., Roth, G., & Rudari, R. (2005). A procedure for drainage network identification from geomorphology and its application to the prediction of the hydrologic response. *Advances in Water Resources*, *28*(6), 567–581.

Giosan, L., Syvitski, J., Constantinescu, S., & Day, J. (2014). Climate change: Protect the world's deltas. *Nature*, *516*(7529), 31–33.

Güneralp, I., Filippi, A. M., & Hales, B. U. (2013). River-flow boundary delineation from digital aerial photography and ancillary images using support vector machines. *GIScience & Remote Sensing*, *50*(1), 1–25. https://doi.org/10.1080/15481603.2013.778560

Hancock, G., & Evans, K. (2006). Channel head location and characteristics using digital elevation models. *Earth Surface Process and Landforms*, *31*(7), 809–824.

Homer, C., Dewitz, J., Fry, J., Coan, M., Hossain, N., Larson, C., et al. (2007). Completion of the 2001 national land cover database for the conterminous United States. *Photogrammetric Engineering and Remote Sensing*, *73*, 337–341.

Howard, A. D., Keetch, M. E., & Vincent, C. L. (1970). Topological and geometrical properties of braided streams. *Water Resources Research*, *6*(6), 1674–1688.

Isikdogan, F., Bovik, A., & Passalacqua, P. (2015). Automatic channel network extraction from remotely sensed images by singularity analysis. *IEEE Geoscience and Remote Sensing Letters*, *12*(11), 2218–2221.

Isikdogan, F., Bovik, A., & Passalacqua, P. (2017a). RivaMap: An automated river analysis and mapping engine. *Remote Sensing of Environment*, *202*, 88–97.

Isikdogan, F., Bovik, A. C., & Passalacqua, P. (2017b). Surface water mapping by deep learning. *IEEE Journal of Selected Topics in Applied Earth Observations and Remote Sensing*, *10*(11), 4909–4918.

Isikdogan, F., Bovik, A., & Passalacqua, P. (2019). Seeing through the clouds with deepwatermap. *IEEE Geoscience and Remote Sensing Letters*. https://doi.org/10.1109/LGRS.2019.2953261

Kim, W., & Jerolmack, D. J. (2008). The pulse of calm fan deltas. *The Journal of Geology*, *116*(4), 315–330. https://doi.org/10.1086/588830

Kim, W., Sheets, B. A., & Paola, C. (2010). Steering of experimental channels by lateral basin tilting. *Basin Research*, *22*(3), 286–301. https://doi.org/10.1111/j.1365-2117.2009.00419.x

Lashermes, B., Foufoula-Georgiou, E., & Dietrich, W. E. (2007). Channel network extraction from high resolution topography using wavelets. *Geophysical Research Letters*, *34*, L23S04. https://doi.org/10.1029/2007GL031140

McFeeters, S. (1996). The use of normalized difference water index (NDWI) in the delineation of open water features. *International Journal of Remote Sensing*, *17*, 1425–1432.

Merwade, V. M. (2007). An automated GIS procedure for delineating river and lake boundaries. *Transactions in GIS*, *11*(2), 213–231.

Monegaglia, F., Zolezzi, G., Güneralp, I., Henshaw, A. J., & Tubino, M. (2018). Automated extraction of meandering river morphodynamics from multitemporal remotely sensed data. *Environmental Modelling and Software*, *105*, 171–186.

Montgomery, D. R., & Dietrich, W. E. (1988). Where do channels begin? *Nature*, *336*(6196), 232–234.

Montgomery, D., & Foufoula-Georgiou, E. (1993). Channel network source representation using digital elevation models. *Water Resources Research*, *29*(12), 3925–3934.

Muralidhar, G. S., Bovik, A. C., & Markey, M. K. (2013). A steerable, multiscale singularity index. *IEEE Signal Processing Letters*, *20*(1), 7–10. https://doi.org/10.1109/LSP.2012.2226027

Ninomiya, Y. (2004). Lithologic mapping with multispectral ASTER TIR and SWIR data. *Proceedings of SPIE - The International Society for Optical Engineering*, *5234*, 180–190.

Otsu, N. (1979). A threshold selection method from gray-level histograms. *IEEE Transactions on Systems, Man, and Cybernetics*, *9*(1), 62–66. https://doi.org/10.1109/TSMC.1979.4310076

Passalacqua, P., Do Trung, T., Foufoula-Georgiou, E., Sapiro, G., & Dietrich, W. (2010). A geometric framework for channel network extraction from lidar: Nonlinear diffusion and geodesic paths. *Journal of Geophysical Research*, *115*, F01002.

Pavelsky, T. M., & Smith, L. C. (2008). RivWidth: A software tool for the calculation of river widths from remotely sensed imagery. *IEEE Geoscience and Remote Sensing Letters*, *5*(1), 70–73.

Pekel, J., Cottam, A., Gorelick, N., & Belward, A. (2016). High-resolution mapping of global surface water and its long-term changes. *Nature*, *540*(7633), 418–422. https://doi.org/10.1038/nature20584

Pelletier, J. (2013). A robust, two-parameter method for the extraction of drainage networks from high-resolution digital elevation models (DEMs): Evaluation using synthetic and real-world DEMs. *Water Resources Research*, *49*, 75–89. https://doi.org/10.1029/2012WR012452

Powell, E. J., Kim, W., & Muto, T. (2012). Varying discharge controls on timescales of autogenic storage and release processes in fluvio-deltaic environments: Tank experiments. *Journal of Geophysical Research*, *117*, F02011. https://doi.org/10.1029/2011JF002097

Reitz, M. D., Jerolmack, D. J., & Swenson, J. B. (2010). Flooding and flow path selection on alluvial fans and deltas. *Geophysical Research Letters*, *37*, L06401. https://doi.org/10.1029/2009GL041985

Rowland, J. C., Shelef, E., Pope, P. A., Muss, J., Gangodagamage, C., Brumby, S. P., & Wilson, C. J. (2016). A morphology independent methodology for quantifying planview river change and characteristics from remotely sensed imagery. *Remote Sensing of Environment*, *184*, 212–228.

Sangireddy, H., Stark, C. P., Kladzyk, A., & Passalacqua, P. (2016). GeoNet: An open source software for the automatic and objective extraction of channel heads, channel network, and channel morphology from high resolution topography data. *Environmental Modelling and Software*, *83*, 58–73.

Schwendel, A. C., Nicholas, A. P., Aalto, R. E., Sambrook Smith, G. H., & Buckley, S. (2015). Interaction between meander dynamics and floodplain heterogeneity in a large tropical sand-bed river: The Rio Beni, Bolivian Amazon. *Earth Surface Processes and Landforms*, *40*(15), 2026–2040.

Schwenk, J., Khandelwal, A., Fratkin, M., Kumar, V., & Foufoula-Georgiou, E. (2017). High spatiotemporal resolution of river planform dynamics from Landsat: The RivMAP toolbox and results from the Ucayali River. *Earth and Space Science*, *4*(2), 46–75. https://doi.org/10.1002/2016EA000196

Spearman, C. (1904). The proof and measurement of association between two things. *The American Journal of Psychology*, *15*(1), 72–101.

Tarboton, D., Bras, R., & Rodriguez-Iturbe, I. (1988). The fractal nature of river networks. *Water Resources Research*, *24*(8), 1317–1322.

Tucker, C. J. (1979). Red and photographic infrared linear combinations for monitoring vegetation. *Remote Sensing of Environment*, *8*(2), 127–150.

Van Dijk, M., Postma, G., & Kleinhans, M. G. (2009). Autocyclic behaviour of fan deltas: An analogue experimental study. *Sedimentology*, *56*(5), 1569–1589. https://doi.org/10.1111/j.1365-3091.2008.01047.x

Vogelmann, J. E., Howard, S. M., Yang, L., Larson, C. R., Wylie, B. K., & Van Driel, N. (2001). Completion of the 1990's national land cover database for the conterminous United States from Landsat Thematic Mapper data and ancillary data sources. *Photogrammetric Engineering and Remote Sensing*, *67*(6), 650–662.

Xu, H. (2006). Modification of normalized difference water index (NDWI) to enhance open water features in remotely sensed imagery. *International Journal of Remote Sensing*, *27*, 3025–3033.